Experimental description of primary breakup of turbulent rocket engine liquid jet flames

Leonardo Geiger, Nicolas Fdida, Luc-Henry Dorey, Marie Théron, Jean-Bernard Blaisot, Christophe Dumouchel

Experimental description of primary breakup of turbulent rocket engine liquid jet flames

L. Geiger*[1,2,3], N. Fdida[1], L.-H. Dorey[1], M. Théron[3], J.-B. Blaisot[2] and C. Dumouchel[2]

[1]DMPE, ONERA, Université Paris Saclay, F-91123 Palaiseau, France
[2]CORIA, CNRS, Normandie Université, UNIROUEN, INSA ROUEN, Rouen, France
[3]CNES, Space Transportation, Paris, France

Abstract

The present study investigates the primary atomization process of a liquid oxygen/methane powered liquid rocket engine. The study is based on a multi-scale description of the primary liquid ligaments and leads to the determination of their size distribution according to the distance to the injector. The image-based method is improved by using a sub-pixel analysis and a refined surface area measurement technique. Applied to experimental backlighting images obtained at ONERA's MASCOTTE rocket combustor, measurements report that the ligament size distribution increases in average and in dispersion as the distance from the injector increases. The distance at which these liquid structures contain the greatest amount of liquid (and produce therefore the greatest number of drops) is also identified. These results are valuable and may be helpful for the development of numerical simulation models to correctly account for the primary breakup process.

Keywords

Liquid propulsion, assisted atomization, multi-scale analysis, size distribution.

Introduction

The primary atomization of cryogenic propellants in liquid rocket engines (LRE) plays a crucial role in the operation of such engines. It has implications on the efficiency and stability of the combustion process and is strongly linked to engine throttling capacity. The propellants are usually fed into the combustion chamber by a coaxial injection system. In subcritical conditions, the oxidizer is injected as a round liquid jet, whereas the fuel is injected as a high-speed annular gaseous stream. Propellants are considered subcritical when either pressure or temperature (p, T) are lower than their values at the critical point $(p, T)_{crit}$ [1]. Subcritical conditions are found during transient operating phases or nominal operation of throttleable engines, and represent conditions where the combustion process is strongly influenced by the atomization process. Following the gas-assisted atomization regime classification proposed by Lasheras and Hopfinger [2], the injection conditions usually found in LREs correspond to a fiber regime. This regime is characterized by the peeling of the interface that produces fiber-like liquid structures referred to as the textural liquid system since their size is far smaller than the liquid jet diameter. These textural structures are responsible for the production of droplets as they breakup in the vicinity of the liquid jet.

This type of process has been reported on large non-turbulent liquid jets [3]. The size of the droplets produced were shown to correlate with the thickness of the boundary layer developed in the injector. Textural atomization processes were also observed on large turbulent liquid jets [3-5]. In this case, the size of the droplets produced related to the local turbulence scales in the liquid flow. The presence of ligamentous liquid structures may therefore be the result of turbulent fluctuations in the liquid phase, which overcome the surface tension at the liquid-gas interface and cause the ejection of liquid protuberances from the liquid jet [4]. These ligaments may also result from the development of surface instabilities, as reported for air-assisted liquid

jets [6, 7]. In a recent study, a textural atomization process resulting from cavitation effects was studied by measurement of a scale distribution of the liquid ligaments on experimental images [8].

Few studies have focused on the description of textural atomization processes and of the spray resulting from it. The studies cited above all report the production of drops by liquid ligaments at the interface. Under conditions representative of methane/liquid oxygen-powered LRE combustion chambers, the description of the spray is made difficult by the presence of strong density gradients. The description of the liquid ligaments instead allows to study the textural atomization process leading up to the production of drops. The present work aims at describing these textural liquid structures, as visualized in a LRE-type experimental setup. The description method is based on a multi-scale analysis technique [8], which allows quantifying the size distribution of the textural ligaments and its evolution with the distance from the injector exit plane.

Experimental setup

Experiments were performed in a subscale cryogenic rocket combustor capable of reproducing operating conditions similar to those encountered inside the combustion chambers of LREs. ONERA's MASCOTTE test-bench [9] allows the study of fundamental mechanisms taking place inside the combustion chamber of such engines. These include, among others, the injection, atomization and combustion of the propellants, the onset of combustion instabilities, as well as heat transfer and pollutant and soot formation [10-12]. The combustion chamber used during tests is water-cooled and designed to operate at conditions representative of real rocket engine main chambers, i.e., high pressures and high mixture ratios. The injection system is composed of a single shear-coaxial injector, which feeds an oxidizer (liquid oxygen) jet through a central circular tube, while a gaseous fuel (methane) stream is injected through an outer annular tube. There is no recess between the oxygen and the methane injector-tube exit planes.

One single operation condition is considered in this study. The tested operating condition is characterized by a liquid Reynolds number Re_L ~ $7x10^4$, a relative Weber number We_R ~ $3x10^4$, a momentum flux ratio J = 15 and a chamber pressure P_c = 7 bar. The propellants injected into the combustion chamber are therefore in a subcritical state. The oxidizer-fuel mixture is slightly fuel-rich, with a near-stoichiometric mixture ratio (M = 3.5), as is common in LRE main combustion chamber nominal operation [13]. The injection parameters place the current configuration in the fiber-type breakup regime, according to the atomization regime diagram from Lasheras and Hopfinger [2].

The chamber is equipped with two opposite rectangular quartz optical ports of 25 mm x 60 mm that allow the visualization of the atomization and combustion phenomena. A backlighting setup comprised of a laser beam and a camera was employed to record images of the atomization process. This technique consists of visualizing of the shade from the dense liquid phase as light traverses the combustion chamber. The backlighting imaging setup is represented schematically in Fig. 1. The light source used is a Cavilux Smart 400 W laser emitting a red incoherent light pulse of 1-1.5 µs duration and at a wavelength of 640 ± 10 nm. A narrow band filter is used to block the light from the flame emission while allowing the light from the laser source to reach the sensor. The backlit images are recorded at 50 Hz with a JAI GOX-2402 camera, with pixels of 3.45 µm size, equipped with a long-distance microscope Infinity K2 DistaMax with a CF1/B lens. This setup results in a field of view of 8.64 mm x 5.40 mm, with a spatial resolution of 4.5 µm/pixel.

Images were taken at varying positions along the injection axis. Three positions were used to capture the interface in the near-injector region, where the observed textural deformation of

the liquid ligaments is at its most intense. Fig. 2 shows an image of the entire atomization process during liquid oxygen/methane combustion at the MASCOTTE test-bench, with indications to the positions of the near-field, high-resolution images captured and used in this study. The midlines of the near-field images are z = 5.11 mm, z = 13.75 mm and z = 22.39 mm.

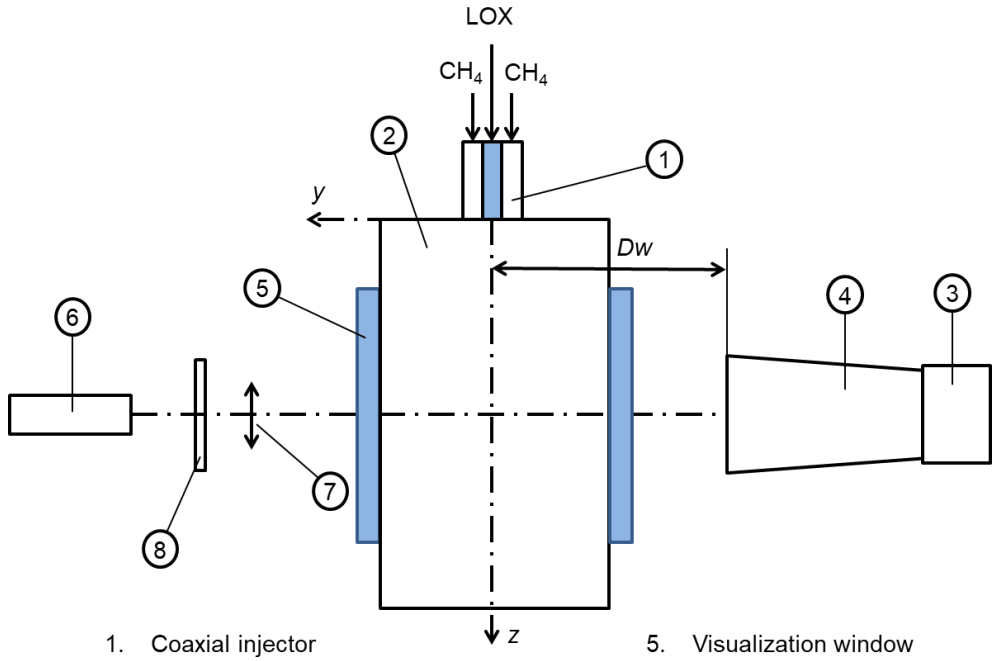

Figure 1 Schematic representation of the backlighting imaging setup.

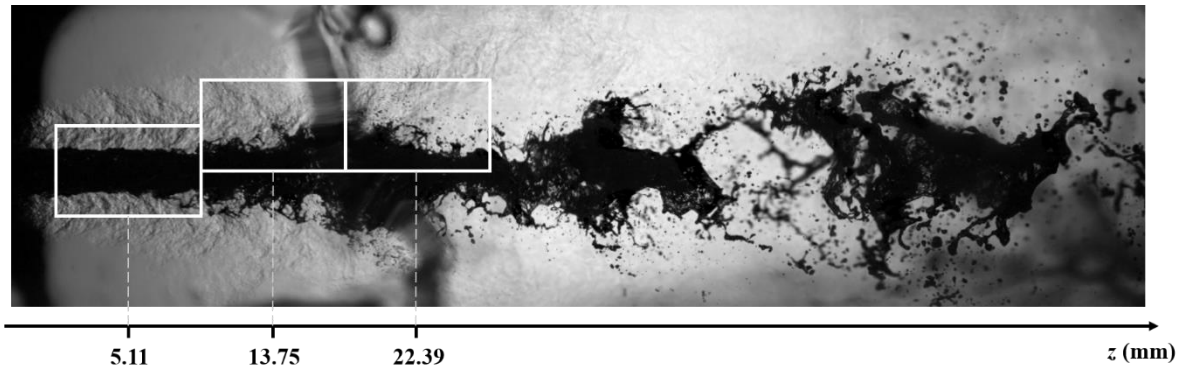

Figure 2 Visualization of the entire optical window showing the atomization process under liquid oxygen/methane combustion in the MASCOTTE test-bench. White rectangles indicate the corresponding positions of the three series of high-resolution images used in this study.

Textural liquid structures multi-scale description

The proposed description of the textural atomization process relies on the multi-scale analysis established in previous works [8, 14, 15]. This method consists in describing a liquid system (as the one obtained from the backlighting imaging of the atomization process described in the previous section) as well as all systems parallel to it inside the liquid phase. These parallel systems are those obtained by erosion operations on the original liquid system. An erosion operation consists of removing from the system a layer of liquid identified by dragging a disk

of diameter *d* along its interface while keeping the center of the disk on the interface line. The liquid system that remains after this operation is called the system eroded at scale *d*. All parallel liquid systems are obtained by performing this operation for all possible values of *d* from 0 to the maximum scale of the liquid system. These liquid systems are described by their surface area $S(d)$, their interface length $L(d)$, and their length-integrated curvature $H(d)$ [15].
The experimental description of the visualized liquid system is based on the measurement of $S(d)$. The details of the corresponding image processing are described in the next section. The function $S(d)$ is used to determine the cumulative scale distribution $E_2(d)$, defined as $E_2(d) = S(0) - S(d)$. The derivative of $E_2(d)$ with respect to the scale *d* is the scale distribution $e_2(d)$, which is proportional to the interface length: $e_2(d) = L(d)/2$ [15]. This work also considers the derivative of the scale distribution, $e_2(d)_{,d}$, representing the variation of the interface length provoked by the erosion of the liquid structures smaller than *d*. It has been shown [8] that the derivative of the scale distribution can be expressed as a mono-modal diameter distribution $f_{0c}(D)$ of an equivalent ensemble of N_c cylinders of constant length L_c:

$$-e_2(d)_{,d} = N_c L_c \left(f_{0c}(D)\right)_{D=d} \tag{1}$$

Equation (1) implies that $-e_2(d)_{,d}$ reports one peak. In addition, since $f_{0c}(0) = 0$, $-e_2(0)_{,d} = 0$ as well. When applied to experimental images of the interface, whose texture is made of ligamentous structures showing a series of contracted or dilated sections, $e_2(d)_{,d}$ yields the distribution of size of these sections.

Image processing and measurements

As detailed in the previous section, to measure the surface areas $S(d)$ of a given liquid system, an Euclidean Distance Map (EDM) is applied on the image. This operation attributes, to each liquid pixel, a brightness level equal to the shortest distance between the pixel and the interface. The surface area $S(d)$ corresponds to the number of pixels with a brightness level equal or larger than $d/2$. Once the surface areas $S(d)$ are measured, the cumulative scale distribution $E_2(d)$ and its successive derivatives $e_2(d)$ and $e_2(d)_{,d}$ can be constructed. The derivation is performed using a central finite difference scheme, and each derivation is preceded by a 3-point moving-average smoothing of the function.
To illustrate the measurement technique, it is applied on the synthetic object shown in Fig. 3. The object represents an 800-pixel-long cylinder of 70 pixels in diameter disturbed by a sinusoidal perturbation of amplitude 31 pixels and wavelength 800 pixel. The theoretical expression for $-e_2(d)_{,d}$ of this system is known [15] and shown in Fig. 4(a), where it is compared with the corresponding measurement. The theoretical $-e_2(d)_{,d}$ shows two discontinuities, one at $d_1 = 8$ pixels corresponding to the diameter of the cylinder contraction, and one at $d_2 = 132$ pixels, corresponding to the diameter of the cylinder swelling. Fig. 4(a) shows relative agreement between the measurement and the theoretical solution. There are, however, significant differences, such as the presence of oscillations in the measurement between scales d_1 and d_2, as well as a poor description of the peaks at the discontinuities. The pixelized nature of the image leads to surfaces $S(d)$ that always correspond to integer numbers of pixels. This induces a bias in the measurement and leads to the oscillations observed between scales d_1 and d_2. In addition, insufficient spatial resolution of the image leads to the imprecise description of the theoretical peaks near these two scales. These differences must be addressed to allow the study of the small-scale features of the interface. Two operations are used to improve the measurements:

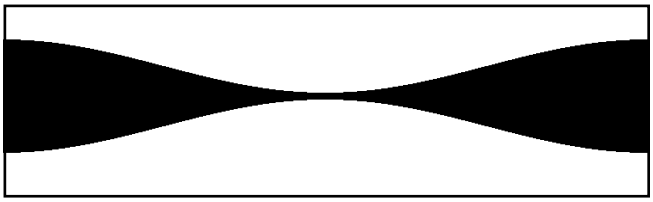

Figure 3 Synthetic cylinder with sinusoidal perturbation.

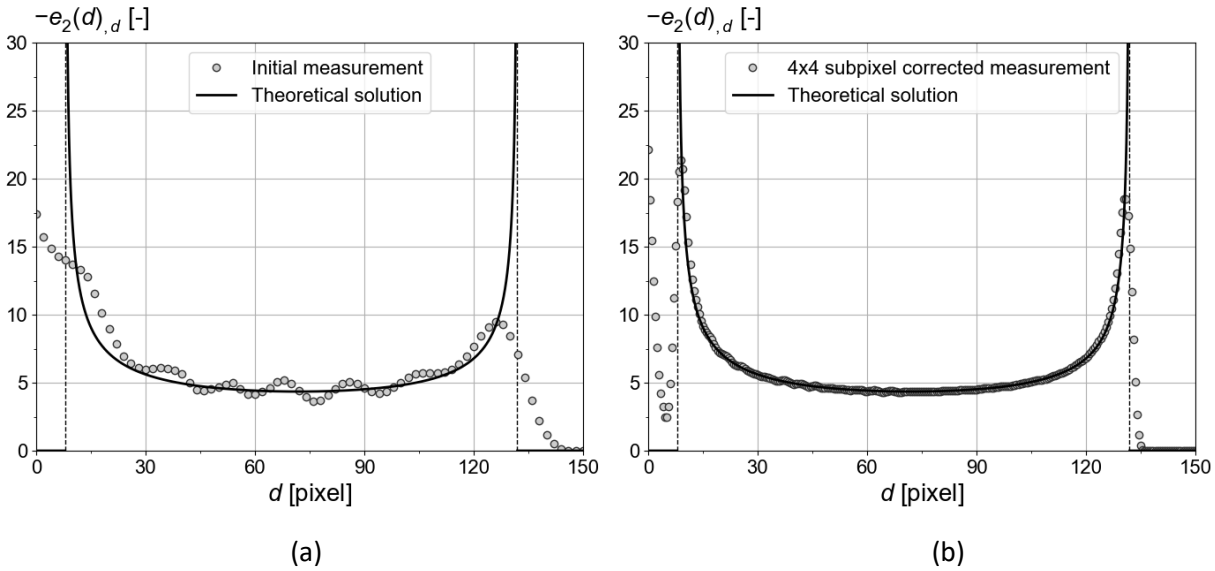

Figure 4 Comparison between the theoretical and the measured distribution $-e_2(d)_{,d}$. (a) Initial measurement, (b) corrected measurement with a 4x4 sup-pixel treatment.

The first is a sub-pixel treatment to increase image resolution. This treatment consists of a bilinear interpolation performed on the pixel brightness levels to increase the number of pixels in the image, therefore increasing its spatial resolution [16]. An NxN interpolation operation results in a division of each pixel into N^2 sub-pixels and in a spatial resolution multiplied by N. The second operation is a correction in the measurement of the surface areas *S(d)*. As mentioned above, these surface areas correspond to the number of pixels with a brightness level equal or larger than *d*/2, as given by the EDM transformation. The EDM algorithm (ImageJ Distance Map function) assigns to each pixel a brightness level (equivalent to the shortest distance between the pixel and the interface) equal to an integer number. However, the exact distance between the pixel and the interface does not always equal an integer number. The EDM algorithm yields a rounded value of the exact distance. The correction proposed here uses the exact distance values given by the EDM algorithm used in the Python *scipy.ndimage.distance_transform_edt* function. The exact distance is defined by

$$r = \sqrt{n_x^2 + n_y^2} \tag{2}$$

where n_x and n_y correspond to the number of pixels separating the considered pixel to the nearest interface pixel as shown in Fig. 5.

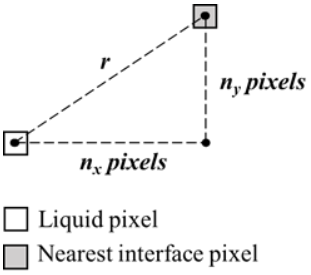

Figure 5 Definition of n_x and n_y.

The resulting distances r are thus a series of discrete values, which can be rewritten as $r = r_I + r_F$, where r_I and r_F are the integer and fractional parts of r, respectively. The exact distance series r is distributed into a new series of integer bins corresponding to the integer parts r_I. The repartition of the exact distances r to the integer-distance series r_I is done according to the following proportion:

$$\begin{cases} (1 - r_F) \text{ in bin } r_I \\ r_F \text{ in bin } (r_I + 1) \end{cases} \quad (3)$$

This means that each pixel, with an exact distance to the interface equal to r, is divided in two parts, with $(1 - r_F)$ feeding the bin r_I and r_F feeding the bin $(r_I + 1)$. Once the contribution of all liquid pixels has been added to their corresponding bins r_I, each bin contains a value equal to the sum of all the fractions of pixels added to it. This value $n(r_I)$ is no longer necessarily an integer. The surface area of the parallel systems at a distance *d*/2 from the interface, *S(d)*, can then be expressed as:

$$S(d) = S(0) - \sum_{r_I=0}^{d/2} n(r_I) \quad (4)$$

which yields non-integer values of *S(d).*

Fig. 4(b) shows the measurement of $-e_2(d)_{,d}$ using both the correction in the surface areas measurement and a 4x4 sub-pixel interpolation. The comparison with the theoretical solution shows that these operations considerably improve the measurements in the entire scale range. Oscillations disappear, the positions of the peaks at the discontinuity scales d_1 and d_2 are accurately captured, and $-e_2(d)_{,d}$ decreases towards zero at scales smaller than d_1. The presence of a peak at $d = 0$ is related to effects of pixelization that have been shifted towards smaller scales compared to the initial measurement. This result indicates the smallest scale resolved by the present measurement process: according to Fig. 4(b), this scale is of the order of 5 pixels.

The considered multi-scale technique requires the use of segmented images where the liquid is shown in black pixels against a white background. To obtain these images, the raw backlighting images undergo a segmentation step to separate the liquid from the gaseous environment. The segmentation is performed using a local Phansalkar thresholding algorithm [17]. The liquid structures detached from the liquid core are eliminated and white holes in the liquid core are filled with black pixels. The experimental backlighting images undergo a 4x4 sub-pixel treatment before segmentation. The results of the application of the multi-scale measurement technique on these images, using the proposed *S(d)* correction and the sub-pixel treatment, are detailed in the next section.

Results and Discussions

Fig. 6 shows snapshots of segmented experimental images at the three captured positions. Gray areas represent parts of the images that could not be used due to visualization limitations from the lighting source or from depositions on the optical window. The liquid-gas interface

shows both large-scale and small-scale disturbances. The large-scale disturbances can be seen in the images as large-wavelength waves and are probably caused by the development of a Kelvin-Helmholtz instability. The small-scale features are associated with the presence of textural, ligament-shaped liquid structures at the interface. Fig. 6 shows that the size, length and quantity of these structures evolve with the distance *z*. As the distance from the injector increases, the structures seem to increase in size and in number. This observation is the same as the ones made by Wu et al. [4] where it has been proposed that these textural ligaments are produced as an effect of the turbulent fluctuations in the liquid. Near the injector, turbulent fluctuations of small scale have enough energy to break the surface tension and lead to the production of thin ligaments. As the distance to the injector increases, the small turbulent eddies dissipate and are no longer able to overcome the surface tension forces. Therefore, as the size of the turbulent eddies required to break the surface tension increases with the distance to the injector, so does the thickness of the produced ligaments, which will in turn result in the production of larger droplets. In addition to the turbulent fluctuations in the liquid phase, the high-speed coaxial gas flow also influences the textural atomization process. It has been shown [4] that the aerodynamic effects caused by the gaseous co-flow become relevant when the density ratio ρ_L/ρ_G is less than 500. The ratio in the current study is of 224. The aerodynamic effects can be identified in Fig. 6 by the streamwise orientation of the liquid ligaments, which is particularly visible near the injector. These effects are associated with a pressure drop caused by the acceleration of the gas around the liquid structures, which contributes to their stretching. In addition, the aerodynamic effects may trigger a secondary breakup of the droplets produced by the textural structures. This secondary breakup is not considered in the current study.

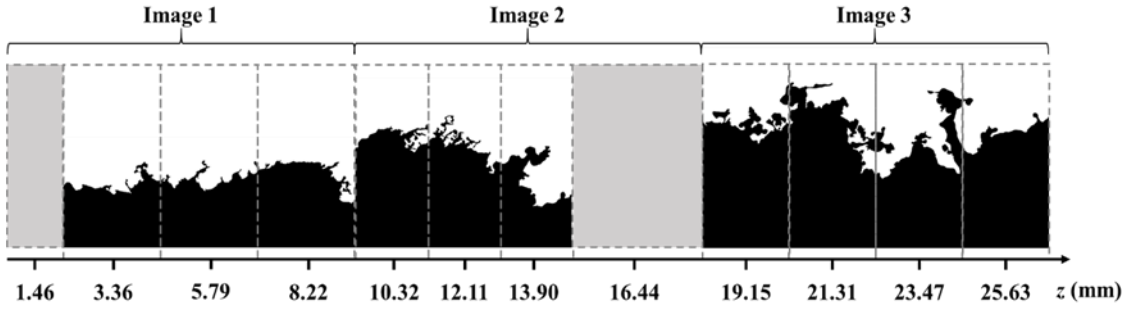

Figure 6 Snapshot of the segmented liquid-gas interface as a function of the distance *z* from the injector exit plane. The liquid phase is represented in black, and only the liquid core interface is shown.

The three experimental backlighting image series are segmented and divided into ten regions of interest (ROI) as a function of the distance *z* from the injector exit plane. Images 1 and Images 2 are divided in three ROI of width 2.43 mm and 1.79 mm, respectively. Images 3 are divided in four ROI of width 2.16 mm. The measurement technique detailed in the previous section is applied to a series of a minimum of 100 decorrelated segmented images for each position *z*. Time-averaged $e_2(d)$ and $-e_2(d)_{,d}$ distributions are obtained for each of the ten ROI shown in Fig. 6.

Fig. 7 shows the resulting average $e_2(d)$ scale distribution at seven different positions. To allow a direct comparison of the results, the distributions are divided by the ROI width w_{ROI}. The distributions are shown in the textural scale range only. Points near $d=0$ are not shown because they contain inaccuracies introduced by image pixelization, as discussed in the previous section. As mentioned in the multi-scale method section, $e_2(d)$ is proportional to the perimeter of the parallel systems at a distance *d* from the liquid-gas interface. At each position *z*, $e_2(d)$ shows a maximum value at the smallest resolved scale (around 20 µm), followed by

a decrease with the scale *d*. This decrease with *d* is due to the erosion of the liquid structures of size smaller than *d*, which leads to a reduction in the perimeter of the eroded system. Past a certain scale, the distributions stop decreasing and become constant with *d*, indicating that the textural liquid structures have been completely eroded. The scale at which each distribution stops changing with *d* (and therefore the size of the largest textural structures) increases with the distance *z* from the injector. This increasing spread of $e_2(d)$ towards larger scales indicates the presence of thicker ligaments as the distance from the injector increases. The value of $e_2(d)$ at the smallest considered scales also evolves with *z*. The distributions show an increase of the interface length until *z* = 21.31 mm, after which the interface length starts decreasing. This represents an increase of the number and/or length of textural ligaments up to the distance *z* = 21.31 mm, where they reach a maximum. At this distance, the textural structures involve the greater amount of liquid (and will produce the greater number of drops).

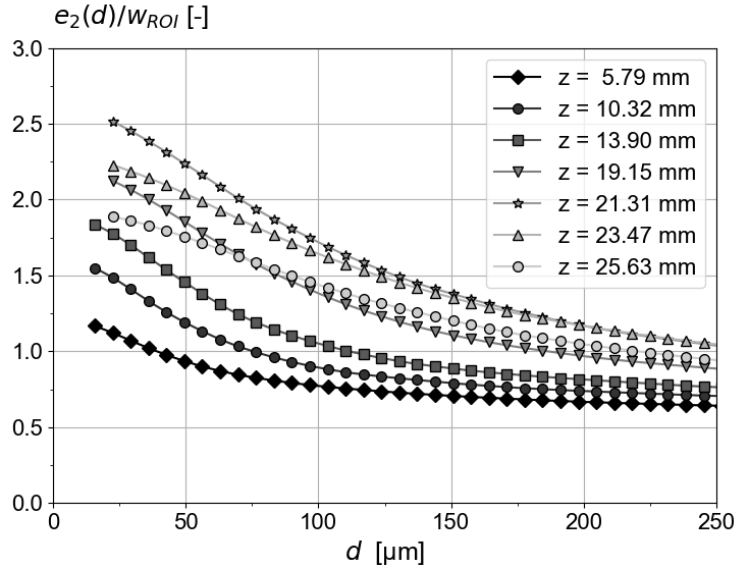

Figure 7 Measurement of $e_2(d)$, divided by the ROI widths, in the textural scale range for six different positions *z*. One in every three points is shown.

Fig. 8 reports the derivative of the scale distributions from Fig. 7. The derivatives $-e_2(d)_{,d}$ have a bell shape and can be interpreted as the diameter distribution of the ligament diameters. It has been shown [15] that the part to the left of the peak mostly represents the distribution of diameters of the contracted sections of the ligaments, while the part to the right of the peak mostly corresponds to the distribution of diameters of the dilated sections. These dilated sections of the ligaments are associated with structures that will potentially breakup into droplets as the atomization process evolves with time. The height of $-e_2(d)_{,d}$ is related to the number of cylinders in the equivalent set of cylinders (see Equation (1)). The integral of $-e_2(d)_{,d}$ over the entire scale range informs on the number and/or length of the ligaments. The position where this integral is maximum corresponds to the position where the textural atomization is the most intense. Fig. 8 shows that the scales where the peaks are positioned increase with *z*. In addition, the distributions spread towards the large-scale zone as *z* increases. This indicates that the diameter of the dilated sections (the sections that will potentially breakup into droplets) increases with the distance *z* from the injector, as can be observed in Fig. 6. The increase of the dispersion of the distributions with *z* indicates the presence of ligaments whose deformations cover a wider diameter range far from the injector. Finally, all distributions approach zero at the large-scale zone, indicating the absence of textural structures of size larger than *d* = 250 µm. The main general observations of the textural atomization process

made on the experimental images are therefore quantitatively described through the refined measurement of local scale distributions of the textural ligaments.

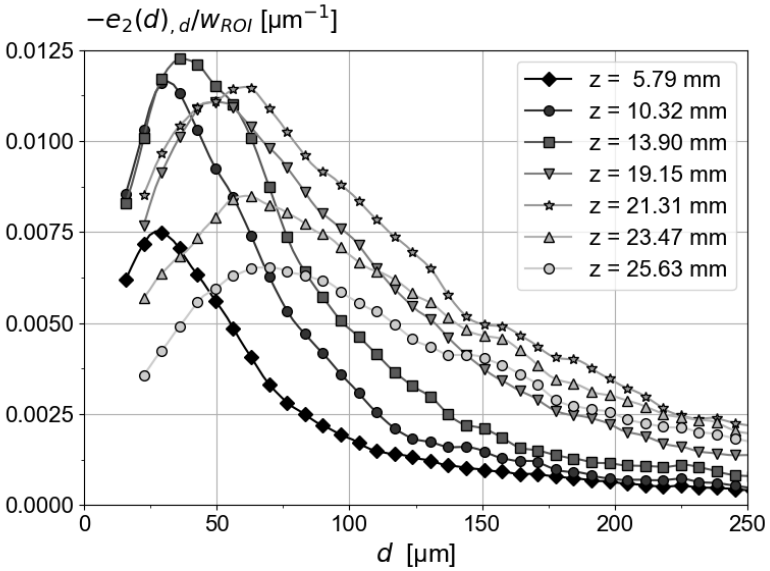

Figure 8 Measurement of $-e_2(d)_{,d}$, divided by the ROI widths, in the textural scale range for six different positions *z*. One in every three points is shown.

Conclusions

The present experimental study aims at a description of the fiber-regime primary atomization process in LRE subcritical and reactive conditions. It demonstrates that the multi-scale description of the visualized liquid jet can be used to describe the textural features of the system in the near-injector region. The multi-scale description is provided by the measurement of a scale distribution $e_2(d)$, and of its derivative $-e_2(d)_{,d}$. Image pixelization effects on the measurements are highlighted for a synthetic object. Two methods are proposed to mitigate these problems. Combined, they allow to describe the visualized liquid system on its entire textural-scale range, including small scales previously unattained. The measurement of time-averaged $e_2(d)$ and $-e_2(d)_{,d}$ distributions provides a description of the amount of interface carried by the textural liquid ligaments as well as of their diameter distribution. Measurements were made on a series of ROIs at different distances from the injector exit plane, covering the region where the textural process is most intense. The spatial evolution of the textural atomization process is reported by the evolution of $e_2(d)$ and $-e_2(d)_{,d}$. The results indicate an increase in the size and deformation of the textural ligaments with the distance from the injector. The results also report an increase in the number and/or length of textural ligaments up to a certain distance (z = 21.31 mm), after which these structures begin to disappear. These results represent an important step towards a more complete description of the textural atomization process, i.e., the description of the characteristics of the droplets produced by the textural liquid structures, and can be used to develop textural atomization models.

References

[1] Mayer, W. O., Schik, A. H., Vielle, B., Chauveau, C., Gokalp, I., Talley, D. G., & Woodward, R. D. (1998). Atomization and breakup of cryogenic propellants under high-pressure subcritical and supercritical conditions. *Journal of Propulsion and Power*, *14*(5), 835-842.

[2] Lasheras, J. C., & Hopfinger, E. J. (2000). Liquid jet instability and atomization in a coaxial gas stream. *Annual review of fluid mechanics*, *32*(1), 275-308.

[3] Wu, P. K., Miranda, R. D., & Faeth, G. M. (1995). Effects of initial flow conditions on primary breakup of nonturbulent and turbulent round liquid jets. *Atomization and sprays*, *5*(2).

[4] Wu, P. K., Tseng, L. K., & Faeth, G. M. (1992). Primary breakup in gas/liquid mixing layers for turbulent liquids. *Atomization and sprays*, *2*(3).
[5] Wu, P. K., & Faeth, G. M. (1993). Aerodynamic effects on primary breakup of turbulent liquids. *Atomization and Sprays*, *3*(3).
[6] Hoyt, J. W., & Taylor, J. J. (1977). Waves on water jets. *Journal of Fluid Mechanics*, *83*(1), 119-127.
[7] Marmottant, P., & Villermaux, E. (2004). On spray formation. *Journal of fluid mechanics*, *498*, 73-111.
[8] Dumouchel, C., Blaisot, J. B., Abuzahra, F., Sou, A., Godard, G., & Idlahcen, S. (2019). Analysis of a textural atomization process. *Experiments in Fluids*, *60*, 1-16.
[9] Habiballah, M., Orain, M., Grisch, F., Vingert, L., & Gicquel, P. (2006). Experimental studies of high-pressure cryogenic flames on the Mascotte facility. *Combustion Science and Technology*, *178*(1-3), 101-128.
[10] Boulal, S., Fdida, N., Matuszewski, L., Vingert, L., & Martin-Benito, M. (2022). Flame dynamics of a subscale rocket combustor operating with gaseous methane and gaseous, subcritical or transcritical oxygen. *Combustion and Flame*, *242*, 112179.
[11] Fdida, N., Vingert, L., Ristori, A., & Le Sant, Y. (2016). Droplet size and velocity measurements in a cryogenic jet flame of a rocket-type combustor using high-speed imaging. *Atomization and Sprays*, *26*(5).
[12] Grenard, P., Fdida, N., Vingert, L., Dorey, L. H., Selle, L., & Pichillou, J. (2019). Experimental investigation of heat transfer in a subscale liquid rocket engine. *Journal of Propulsion and Power*, *35*(3), 544-551.
[13] Preuss, A., Preclik, D., Mading, C., Gorgen, J., Soller, S., Haidn, O., ... & Sender, J. (2008, May). LOx/Methane technology efforts for future liquid rocket engines. In *5th international spacecraft propulsion conference & 2nd international symposium on propulsion for space transportation*.
[14] Dumouchel, C., Thiesset, F., & Ménard, T. (2022). Morphology of contorted fluid structures. *International Journal of Multiphase Flow*, *152*, 104055.
[15] Dumouchel, C., Cottier, L., & Renoult, M. C. (2023). Fine characterization of the capillary instability of free viscoelastic jets. *Journal of Non-Newtonian Fluid Mechanics*, *322*, 105135.
[16] Fadnavis, S. (2014). Image interpolation techniques in digital image processing: an overview. *International Journal of Engineering Research and Applications*, *4*(10), 70-73.
[17] Phansalkar, N., More, S., Sabale, A., & Joshi, M. (2011, February). Adaptive local thresholding for detection of nuclei in diversity stained cytology images. In *2011 International conference on communications and signal processing* (pp. 218-220). IEEE.